Chapter 2
Fabrication of Platforms for Bioengineering Cellular Response

2.1 Introduction

For regenerative medicine, stem cells become a natural choice for cellular therapy because of their potential to differentiate into a variety of lineages, to generate tissue constructs in-vitro, and capacity to self-renew the repair of damaged organs and tissues. Determining the ability to efficiently drive stem cell differentiation to a lineage of choice is critical for the success of cellular therapeutics. Many factors are employed to tune the differentiation process, such as the use of growth factors, growth factor derivatives, small bioactive molecules, and gene manipulation strategies (to control their expression levels) which has been extensively explored. Other tissue engineering approaches have also been used to incorporate growth and morphogenetic factors known to induce lineage commitment of stem cells-into cultures with scaffolding materials, including synthetic and naturally derived biomaterials. Undoubtedly, growth factors-based enriched environment has been used extensively for in-vitro reprogramming of stem cells towards the desired lineage, but biophysical stimulations have also been capitalized to precisely guide stem cell behavior and differentiation process. However, these biochemical-based strategies still have their own inadequacies that cannot be ignored, including maintaining long-term cell viability, minimizing variability in controlled differentiation and teratoma formation.

In recent times, researchers have focused on the identification of a variety of biomaterials to provide a microenvironment that is conducive to stem cell growth and differentiation and that ultimately mimics the in-vivo situation. Compared to biochemical stimuli, biophysical parameters have a longer lifetime and can be easily modelled. Several biophysical cues, such

as micro/nanotopography, stiffness, porosity, wettability, conductivity, and mechanical strength, are considered vital elements that can be tailored to dictate stem cell differentiation fate.

The use of biologically active nanomaterials for growing and controlling cellular function has been extensively explored in last two decades [68-72]. In the past, several strategies have been adopted to make use of functional materials derived from metals, polymers, ceramics, and composites of their different combinations in devices and implants for biomedical applications [73, 74]. Among these, the syntheses of metals and metal oxides through chemical routes have been used for coatings to achieve a wide range of changes in surface properties for biomedical applications [75, 76]. Particularly, the applicability of metals and metal oxides such as titanium oxides with change in structural, chemical and functional properties for biomedical applications have been extensively studied [77-81]. For example, TiO_2 coatings and their composites have attracted attention in cell culture studies for the pre-assessment of material properties such as biocompatibility, antifouling, antiseptic potential etc. [82-84]. All these studies have suggested that there is a need for continuous innovation in the design and preparation of biomaterials that would show improved biocompatibility, corrosion resistance, and other properties [85, 86].

In earlier studies, cellular biocompatibility has been accentuated by use of titanium oxides for different kinds of cells facilitated by better adhesion at interface of titanium oxide nanostructures coatings on different types of substrates [77-81, 87, 88]. However, it is always challenging to achieve precise control over surface chemistry and obtaining desired structures which can determine specific cellular functions [89-93]. Several methods such as surface treatment [94-96], metal ion doping and hydrolysis processes [87] have been devised to achieve desired crystallite phase, morphologies, 2D/3D structures and surface chemistry in

recent times. Recently, growth of 1D/3D nanostructured TiO_2 at various conditions optimized on different substrates and their biocompatibility was tested with osteoblast and HS-5 cells [97]. The use of these nanomaterials for regenerative medicine has been extensively discussed in the literature but the role of such materials in controlling cellular function of stem/progenitor cells is still not understood well. Further advancements in design of functional material and their manufacturing have been carried out for their use in regenerative medicine and diagnostic applications [98-100]. For cell biology studies, the optical nature of the substrates is also important, thus the assembly of TiO_2 on a transparent substrate, such as glass, is essential to study its effect on stem cells (MSCs) for their adhesion and proliferation [101]. Previously, the deposition of TiO_2 thin films on different types of glass surfaces such as quartz, soda lime and microscopic glass slide for non-biological applications have been reported, but their scope remains limited in biomedical studies [102, 103]. Thus, the objective of this study was considered to investigate the role of a bioengineered platform towards the role of energy metabolites during cell-materials interaction, the transparent coatings of TiO_2 were planned on glass substrates having different characteristics.

2.2 Choice of materials for rationalizing their usefulness

In the past, studies had shown the distinct effect of change in material morphology, chemical composition, surface charge polarity, elasticity, and mechanical strength played a vital role in providing a stimulated environment to the stem cells for regulating cell-material interactions hence achieving a variation in intrinsic properties of stem cell leading to either lineage-specific differentiation of stem cells or their self-renewal. Despite extensive studies and remarkable success in optimizing conditions for achieving desired cell differentiation, still, a correlation between the nature of material properties and cellular response is missing. This is

due to the inter-dependence of the wide range of material's physic-chemical properties, which limits the drawing of a correlation between material individual characteristics response with a particular desired cellular outcome. Therefore, the objectives behind rationalizing the choice of materials were based on varying systematically selective properties while maintaining a fair degree of control over other properties. More specifically, two classes of materials were chosen based on the rationale of providing structural support with tunability in controlling crystalline structure, surface charge, and morphologies of the materials. Another choice of materials was based on the materials' polarity characteristics to mimic the extracellular matrix's physiological variations.

In the present study, different metallic and polymeric platforms have been engineered to direct the differentiation of stem cells. The rationale for fabricating metal-based platforms was to exploit their different properties in terms of different electronegativity, valency, and atomic radii. The introduction of dopant in these metallic frameworks was to aid in the stem cell differentiation process. Further, polymeric platforms were designed to explore another category of biomaterials to explore their physicochemical properties that can be promising parameters for controlling stem cell differentiation. Polymeric materials offer a high degree of tunability in their properties with the advantage of being biodegradable. Thereafter, hybrid glycopolymeric material incorporating two different types of functionalities, polar and non-polar, was designed and studied to achieve a higher degree of differentiation while maintaining a reasonable rate of cell proliferation. The study also included fabricating a 3D caged-nanostructure of TiO_2 on platforms to provide better anchorage sites for cell adhesion and enhanced exchange of nutrients with their microenvironment. Platforms of different conductivity were chosen and studied to analyze the charge neutralization, if any, during the differentiation process.

2.3 Coating of TiO_2 and TiO_2 doped with transition metal ions on glass substrates

2.3.1 Coating methodology

Dip coating process in combination with sol-gel method [104] was used for coating of TiO_2 on transparent borosilicate glass slides (2.5×7.6 cm^2) which were purchased from a local supplier of Blue Star. Titanium tetrabutoxide purchased from Sigma-Aldrich was used as a precursor material for coating of TiO_2. Isopropyl alcohol was used as thesolvent to prepare 0.5 M Ti sol from titanium tetrabutoxide which was partially hydrolyzed by adding DI water in presence of HNO_3 (46%). The mixture was stirred gently with magnetic stirrer for 30 min. under controlled humidity conditions and then it was kept overnight in a vacuum system. Before coating, the microscopic glass slides were placed in a chromic acid cleaning solution for 1 hr and thereafter rinsed for 5 minutes under the tap water. Further, these slides were rinsed with normal cleaning detergent, distilled water, and finally were rinsed in iso-propanol. TiO_2 films were prepared on clean borosilicate glass substrates by sol-gel dip coating process [104] at a pulling speed of 15 cm/min. The film-deposited substrates were dried at 100 °C for 30 min and subsequently annealed at 400 °C for 1hr in normal atmospheric conditions.

Further, to modify the properties of surface of TiO_2, doping with transition metal ions (Ni, Au and La) was done. To obtain Ni doping into TiO_2 thin films, calculated amount of Ni (5 wt. % mole) was added to the prepared Ti sol. Initially the Ni-doped TiO_2 film deposited on the substrates were dried at 100 °C for 30 min and were subsequently annealed at similar temperatures for 1hr in normal atmospheric conditions. The same process has also been adopted for Au and La doping where gold chloride and lanthanum chloride were used as dopant with 5 wt. % mole of these dopants into TiO_2, respectively.

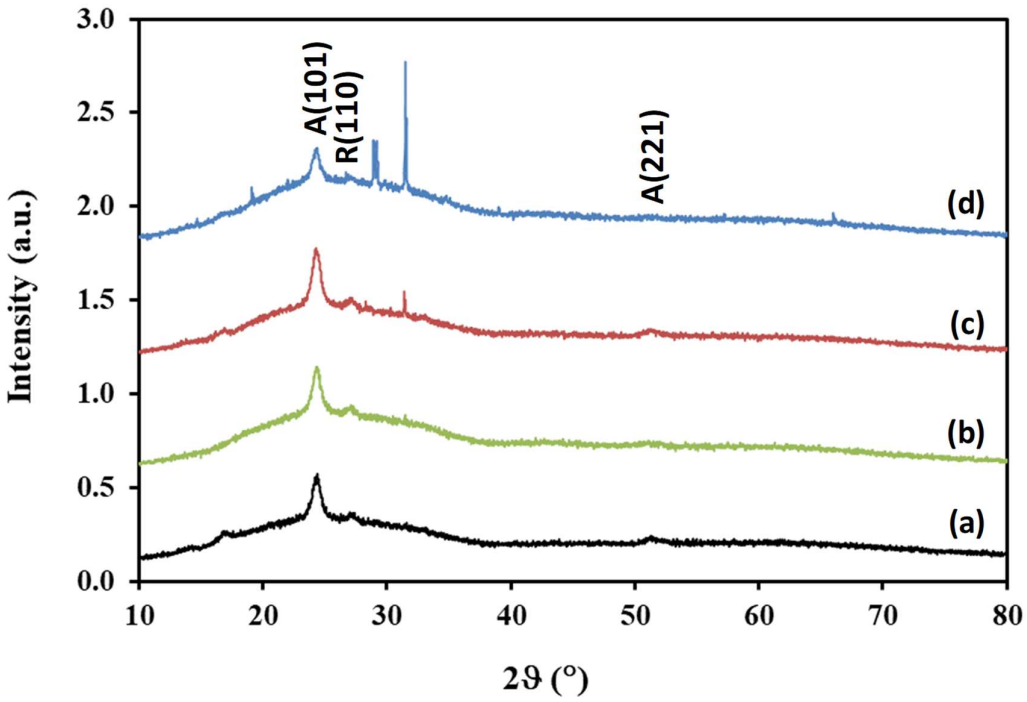

Figure 2.1: XRD spectra of (a) TiO_2 thin films coated on transparent glass surface doped with (b) Ni, (c) Au and (d) La.

2.3.2 Physico-chemical properties

X-ray diffraction patterns of TiO_2 and TiO_2 doped with Ni, Au and La coated surface were recorded at room temperature and results are shown in **Figure 2.1.** XRD spectra of the samples were recorded using a Rigaku Miniflex 600 Desktop X-Ray Diffraction system operated with Cu Kα radiation (λ = 0.15418 nm). Diffraction patterns were recorded over a 2θ range of 5°-80° in continuous mode with a step width of 0.02. Prominent diffraction peaks of undoped TiO_2 observed at 24.9 and 27.6 of 2θ value can be assigned to anatase A (101A) and rutile R(110) phase. The different patterns were mainly dominated by anatase phase as peak corresponds to rutile

phase represented with a very low quantity. Prominent diffraction peaks of Ni doped TiO_2 films are observed at 2θ value of 24.93 and the peak was assigned to reflections from A (101)

crystal plane which also corresponds to dominate anatase (A) phase of TiO_2. Similar observations were also obtained for the diffraction peaks of Au and La doped TiO_2 films at similar values of 2θ value assigned to reflections from A (101) crystal plane. A small intensity XRD peak associated with R (110) plane at 27.6 of 2θ value was also observed for all doped TiO_2 coated surfaces. However, the relative intensity for this peak was highest for the Au doped TiO_2. The XRD peak spectra of doped surface also shows an unidentified peak around 33 of 2θ value which could be attributed to residue of the precursors used during the deposition of the doped TiO_2 film. A noticeable change in the peak broadening was observed in case of doped films which indicates decrease in the size of crystal plane. The average particle size of TiO_2 was estimated by Debye-Scherer equation ($D = (\alpha \lambda) / (\beta \cos\theta)$, where D is mean particle size, α geometric factor is a constant (0.89), λ is x-ray wavelength (1.541 A^o) and β is half width of diffraction peak. The average XRD-based calculated particle size was found between ~ 5 to 20 nm.

The FTIR spectra of films in ATR mode were recorded within a range of 500 – 4000 cm^{-1} with a spectral resolution of 4 cm^{-1} and 64 number of scans using Thermo Scientific Nicolet iS5 at normal incidence. In ATR- FTIR (**Figure 2.2**) observations, transmission peak around 3480 cm^{-1} corresponds to -OH functional group which elevated by doping of Au in TiO_2. This confirms that the structure formation in TiO_2 supports attachment of hydroxyl functional group in the similar way achieved by the Au doping. In contrast to Au doping, the doping of La had decreased the relative proportions of -OH functional group. The doping of Ni showed relatively less change in the hydroxyl group in the spectra. A characteristic peak of –N-H at around 1550 cm^{-1} was also seen in all the samples and all dopants showed significant change in the relative proportion of it as compared to the TiO_2 surface [105].

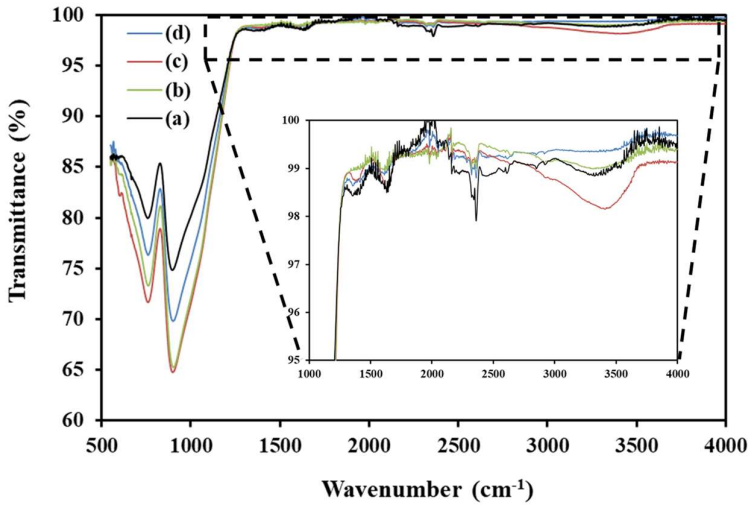

Figure 2.2: ATR spectra of (a) TiO_2 thin films coated on transparent glass surface doped with (b) Ni, (c) Au and (d) La.

FTIR spectrum indicates significant chemical changes in the surface chemistry by film surface prepared by doping of transition metal ions into TiO_2. In addition to this, a strong adsorption peak around 650 cm^{-1} is associated with Si-O which indicates that TiO_2 films have good adhesion to glass substrates [105]. Another interesting characteristic was the decrease in transmutation in the region below 1000 cm^{-1} on the doped film surface and this increase was highest for Ni and Au doping and lowest for La doping in TiO_2.

Quantitative elemental analysis on the TiO_2 thin film coated glass surfaces without and with doping was performed on the X-ray photoelectron spectra (XPS). The XPS were obtained using X-ray photoelectron spectroscopy (XPS) with ESCLAB Xi+, Thermo Fisher Scientific (UK). Survey spectra were acquired at constant pass energy and the elemental quantification was carried out using computer-aided surface analysis software for XPS data analysis. Lower pass energy was used for high-resolution scans of core levels of carbon, oxygen and titanium. Different surface states quantification in the XPS spectra were carried out by specifying a line shape, relative sensitivity factor, position, full width half maxima and area constraints.

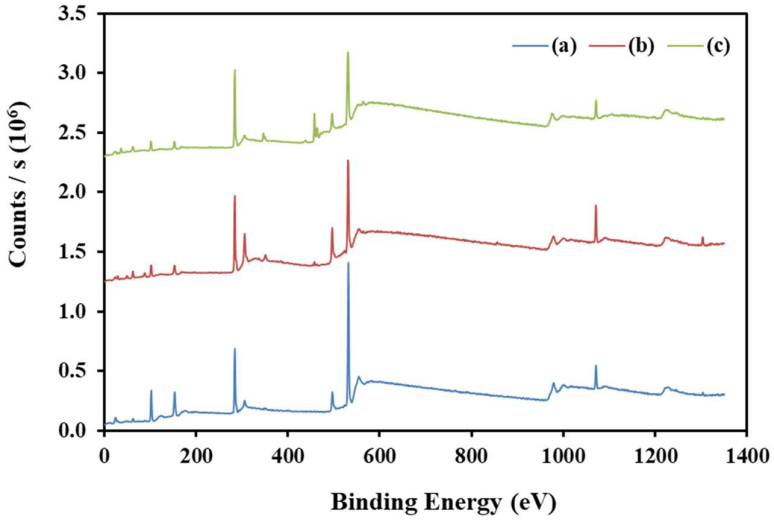

Figure 2.3: XPS wide scan spectra of (a) TiO_2 thin films coated on transparent glass surface doped with (b) Ni and (c) Au.

XPS spectra used to confirm the presence of dopant at film surface and all related results are shown in **Figure 2.3**. The percent atomic concentration of gold (Au), lanthanum (La), nickel (Ni), titanium (Ti), oxygen (O) and carbon (C) was obtained and were tabulated with their relative atomic % atomic proportion in **Table 2.1**.

The presence of Au and Ni proportion at the film surface has been observed in doping of relevant transition metal ions into TiO_2 film surface. The O/Ti values for doped conditions was found to be decreased as compared to TiO_2. Thus, the relative content of oxygen at the film surface had been regulated due to the doping of these transition metal ions. Some carbon content was also seen at the film surface due to the hydrocarbon sassociated with sol-gel process. The C/Ti ratio also decreased in the doping condition as compared to the TiO_2. Based on these findings by XPS elemental analysis, the relative proportion of Au and Ni on the film surfaces appears to be less than 1% for 5 mole % doping in solution and it had decreased surface carbon content which is similar to previously reported findings [104]. To confirm the

***Table 2.1**: XPS elemental analysis showing atomic % proportions of different elements at undoped and doped TiO_2 film surfaces.*

Atomic %	TiO_2	Ni-TiO_2	Au-TiO_2
O1s	47.12	35.93	32.23
C1s	51.65	61.84	62.41
Ti2p	1.23	1.89	5.14
Ni2p	0	0.34	0
Au4f	0	0	0.22

above observation, it was essential to look into the functional diversity of carbon coverage of the doped TiO_2 film surface.

However, it is difficult to correctly quantify the relative number of carbon atoms on the surface of the thin films deposited but high resolution XPS spectra can provide us quantitative information about surface oxidation states. **Figure 2.4** shows the high-resolution C1s XPS spectra for TiO_2 and doped it with Au and Ni. The position of C-C/C-H in C1s spectra remains unchanged and it appears to be at 284.6 eV of the binding energy. C1s peak of Ni doped TiO_2 XPS spectra shows an additional peak at 288 eV which might be due to [-C(=O)OX] carboxylic group at the surface. A small proportion of this peak was also seen for only TiO_2, however, it appears to be completely disappearing for Au doped TiO_2. These observations are very interesting as in the case of Ni doping the appearance of an additional peak might be possibly of Ni, acting as a catalyst to decompose the carbon component incorporated into the film during the sol-gel process and retention of the oxygen functional groups [106].

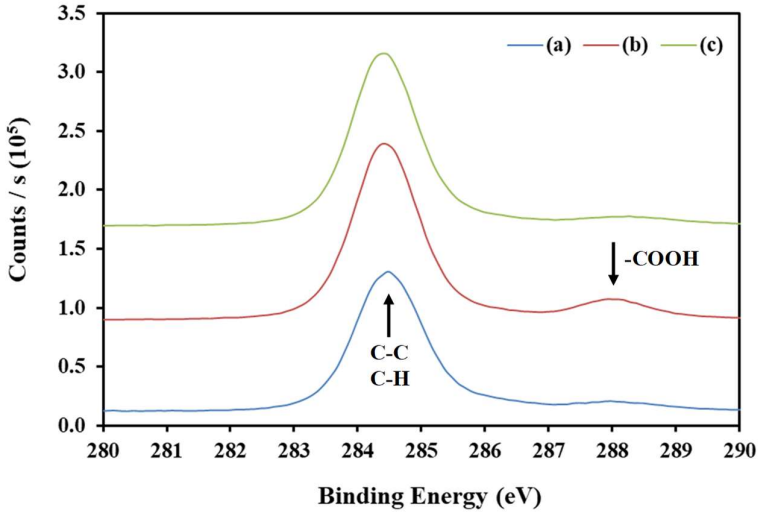

Figure 2.4: XPS C1s spectra of (a) TiO_2 thin films coated on transparent glass surface doped with (b) Ni and (c) Au.

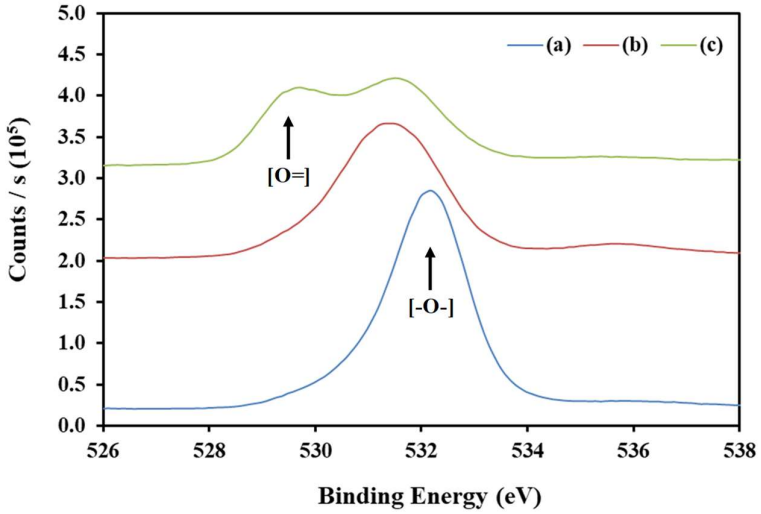

Figure 2.5: XPS O1s spectra of (a) TiO_2 thin films coated on transparent glass surface doped with (b) Ni and (c) Au.

Figure 2.5 shows the O1s narrow scan XPS spectrum of doped and undoped TiO_2. The undoped TiO_2 dominated by the oxygen functionality represented as [-O-] whereas doping with Au showed two distinct peak positions corresponding to [O=] and [-O-] two different

oxidation states. The doping of Ni makes it shift the peak slightly at the lower side of the binding and relative increase in the broadening corresponding to the [-O-] peak.

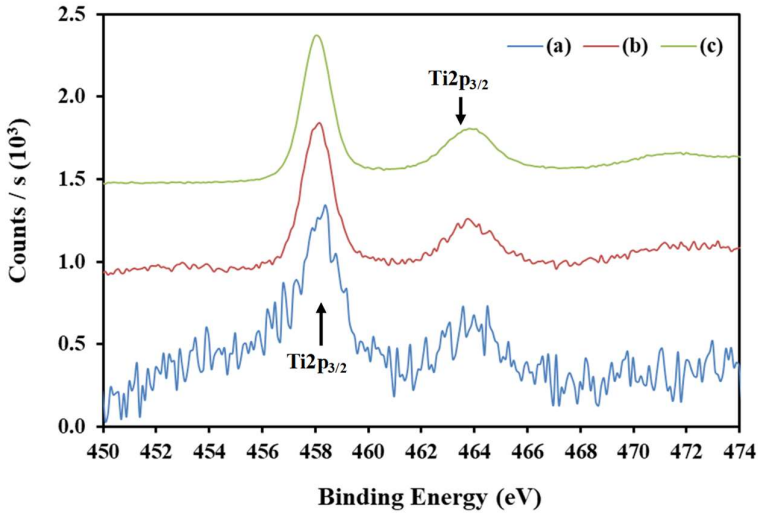

Figure 2.6: XPS Ti2p spectra of (a) TiO_2 thin films coated on transparent glass surface doped with (b) Ni and (c) Au.

Figure 2.6 shows Ti2p spectrum of different conditions of coating on glass substrates prepared by TiO_2 with and without doping with Au and Ni. The spectra has two distinct peaks of Ti represented as $Ti2p_{3/2}$ and $Ti2p_{1/2}$. This is because in XPS spectra, the Ti2p line shape can be described adequately by two peaks which was assigned to the spin-orbit doublet $Ti2p_{3/2}$ and $Ti2p_{1/2}$ for the TiO_2 chemical state [107]. Therefore, to have detailed quantitative analysis of different Ti surface-states at the surface, relative variation in the surface oxidation state is important in determining the chemical characteristics of the coating of TiO_2.

The above results confirm that the crystallite structure of TiO_2 in the coating remains largely unchanged by the doping of the transition metal ion used in this study. However, the chemical characteristics represented by the presence of different proportions of hydroxyl, carboxyl, oxidation states of oxygen were modulated by a great extend due to the use of different metal

ion doping. Thus, these provided conditions where without changing the structure of the materials, variation in the characteristics and composition can be used to study their selective effect on cellular response. Due to the transparent nature of the surface, these are suitable to examine the adhesion, proliferation, differentiation and migration of cells on the surface. It was also possible to use these surfaces to perform studies about investigating localized intracellular cytoskeletal protein interactions on these surfaces.

2.4 Developing engineered 3d-nanostructured TiO_2

2.4.1 Methodology

In the last few years, the main focus of the research was to increase the surface area to volume ratio by developing micro/nanostructures with highly oriented rod-like crystals of TiO_2 for different applications [108-114]. Previously, several studies had shown successful synthesis of 1D TiO_2 as nanowires, nanocorals, nanorods, hierarchical microspheres and nanotubes. Other examples consisting of bilayer coating of TiO_2 having specific structure as nanowire and nanorod without change in their crystallite structures on different substrates is also possible to prepare [115]. Similarly, a combination of 1D nanowire and 3D dendritic TiO_2 nanostructures were also separately coated in multi-step processes on FTO [116]. A process for simultaneous growth of 1D/3D nano-morphologies of TiO_2 has been also developed for achieving desired nanostructures for the application in dye-sensitized solar cells [87]. All these surface changes were achieved with their application in improving their usability in solar cells and other engineering applications. Whereas, their uses in the field of biomedical engineering are not explored yet with their potential in providing controlled external stimulation to stem cells for regulating their fate in self-renewal differentiation.

A surfactant-free one-step hydrothermal process for simultaneous growth of 1D/3D nano-morphologies of TiO_2 has been adopted. This may have the advantage of avoiding the presence of surfactant ad the simultaneous growth of different types of structures such as 1D nanorods and 3D nanoflowers may support tailoring surface morphological characteristics without much alteration in their chemical characteristics for better cellar responses [97]. Previously, the effects of different reaction parameters such as pH, reaction time and temperatures were optimized to grow unique TiO_2 nanostructures as films on different substrates [87, 97]. 3D-TiO_2 nanostructured on two different types of glass, one is plain glass (NCS) and other is conducting glass with an ITO coating (CS), substrates were prepared using titanium isopropoxide solution in 50% diluted hydrochloric acid (HCl). The solution was kept for stabilizing for 1 h and then it was heated at 180°C for 3h. Further, after heating, the substrates were allowed to cool down to room temperature as described previously and then were dried in a vacuum dryer overnight.

The strategy for growth of 3D-nanostructrures of TiO_2 on conducting and non-conducting substrates (CS and NCS) under control hydrolysis, temperature and pressure conditions was to develop platforms of TiO_2. The selection of CS and NCS was based on the hypothesis that conducting nature of CS may allow stem cell to participate in a dynamic process for charge neutralization/spreading across the material surface, whereas NCS and previously used such conditions may limit such stimulation. The dynamic process of continuous alteration in the cell surface charge on stem cells, grown on CS, in response to specific substrates and growth conditions may enforce activation of the specific transcription factors that might enable higher yield of selective differentiation of stem cells.

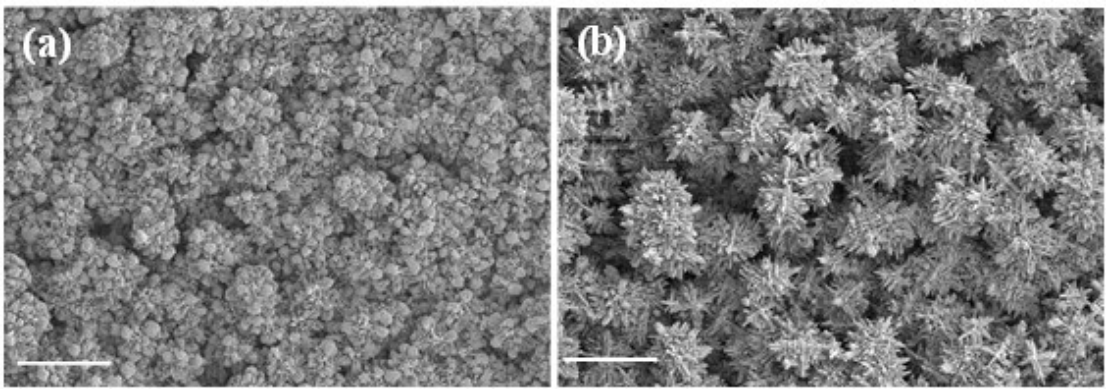

Figure 2.7: SEM image of nanostructured TiO_2 showing surface morphology resembling with flower-like structures of an average size of 8-15 µm and uniform distribution on (a) NCS and (b) CS.

2.4.2 Characterisation of Crystallite Structure and Surface Morphology

The surface morphology of TiO_2 nanostructures on NCS and CS was assessed by scanning electron microscopy (SEM) (**Figures 2.7**). The surface morphology clearly indicates unique structures of TiO2 assembly in a systematic way. The structures resemble unique combination of growth of 3D structure with a larger extend of porosity under these structures. Thus, it looks like a flower which might initially have started growing on singular structure that develops and extends in 3 dimensions and finally results into a unique combination of it.

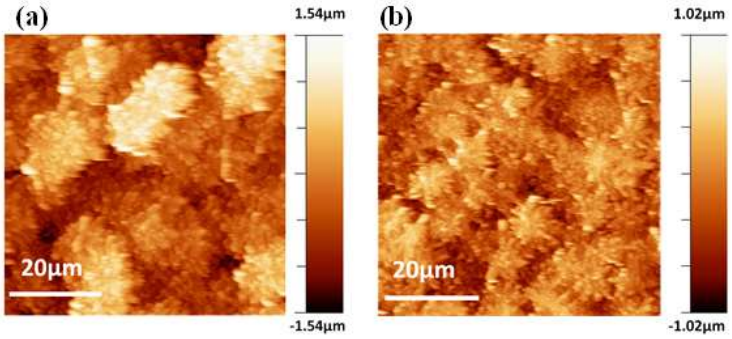

Figure 2.8: AFM image of 3D-nanostructured TiO_2 grown on (a) NCS and (b) CS.

Further, the topographic view in 3D of these structures were examined by atomic force microscopy (AFM) (**Figures 2.8**). Both SEM and AFM analysis confirmed uniform distribution of nanostructures of TiO_2 on CS and NCS which appeared to be three-dimensional nanoporous structures resembling like a flower of an average size of 8-15 µm with 2-3 µm height.

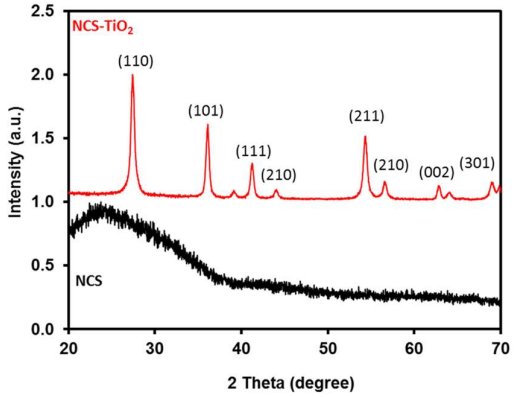

Figure 2.9: XRD spectra of 3D-nanostructured TiO_2 grown on non-conducting surface.

Figure 2.9 shows XRD pattern of TiO_2 nanostructures grown on glass substrates (NC). TiO_2 nanostructures obtained showed XRD peaks appears at 2 theta values of 27.6, 36.3, 41.4, 44.2, 54.6, 56.7, 63.1, 69.3. These peaks were assigned (hkl) values (110), (101), (111), (210),

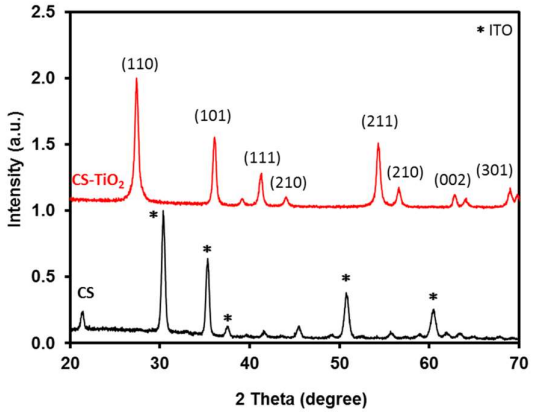

Figure 2.10: XRD spectra of 3D-nanostructured TiO_2 grown on conducting surface.

(211), (220), (002) and (301), respectively. All the diffraction peaks were marked to pure tetragonal rutile phase of TiO_2 (JCPDS no. 21–1276). **Figure 2.10** shows the XRD pattern of TiO_2 nanostructures grown on conducting substrate (CS). ITO substrate shows several strong peaks in XRD spectra as measured previously [102]. TiO_2 nanostructures obtained on CS have similar XRD peaks which appear with the coating on NCS substrates at 2 theta values of 27.6, 36.3, 41.4, 44.2, 54.6, 56.7, 63.1, 69.3. All the diffraction peaks were marked to the pure tetragonal rutile phase of TiO_2. XRD pattern of the TiO_2 nano-structures as films were grown on these two substrates are identical. The contact angle on these surfaces was also measured and nanostructured TiO_2 showed super hydrophilicity on the surface (water contact angle <5°). Raman spectra of nanostructured TiO_2 on CS and NCS shows three Raman active modes at 237.5, 445.2 and 608.5cm^{-1} (**Figure 2.11**), at approximately similar positions for both the materials. These Raman modes are corresponding to rutile crystallinity of TiO_2 [117]. The phase pure rutile nature of TiO_2 nanostructures (grown on CS and NCS) has been confirmed earlier by X-ray diffraction pattern as shown in **Figure 2.9** and **Figure 2.10**.

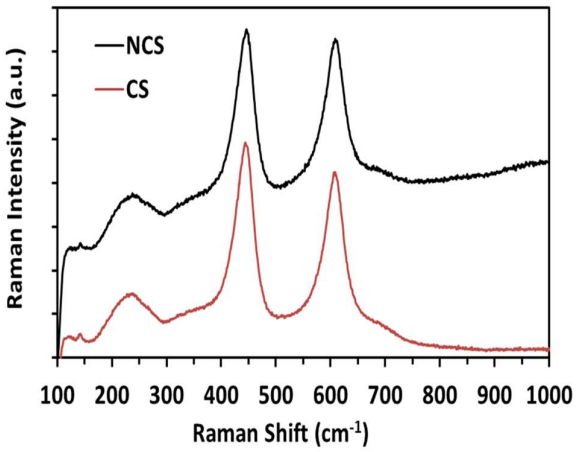

Figure 2.11: Raman spectra of 3D-nanostructured TiO_2 on NCS and CS.

Cyclic voltammetry (CV) response of nanostructured TiO_2 on these surfaces was quantified to assess the charge conductivity in liquid solutions using a three-electrode system. At positive bias voltage, during CV acquisition, charge conduction in TiO_2 nanostructured on CS showed a linear increase in current with the increase of applied voltage. We did not observe any distinct oxidation peak for the TiO_2 on CS which indicates the charge stability of the nanostructured TiO_2 in electrolyte during the applied potential. During the negative bias voltage, we observed a slow increase in the current for the potential below -0.2V. We did not observe significant change in the current of the CV response for the nanostructured TiO_2 on NCS during both positive and negative bias voltages. Thus, nanostructured TiO_2 on CS facilitates dynamic charge neutralization of the TiO_2 surface while interacting with the overlying adhered hHPCs during trans-differentiation into iPCs, as reported in this study.

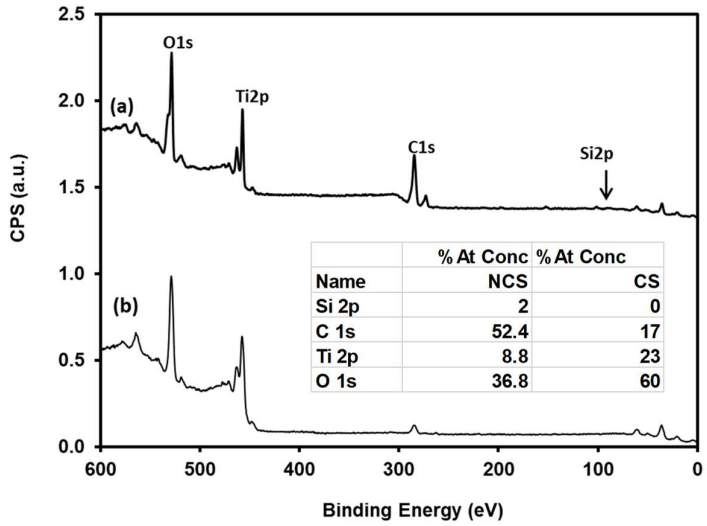

Figure 2.12: Wide scan XPS spectra of TiO_2 on (a) NCS and (b) CS.

2.3.3 Characterization of Surface Chemical Functionalities

Figure 2.12 shows XPS spectra of TiO_2 nanostructure surfaces were obtained for quantification of surface elemental analysis. The % proportions of oxygen (O) to titanium (Ti) atoms were obtained from wide scan XPS spectra. The O/Ti value was 2.7 for the TiO_2 nanostructure surfaces. This observation also indicates that titania atoms are tightly packed at the surface which is also confirmed SEM observations. High resolution XPS spectra of nanostructures grown as films on conducting and non-conducting glass substrates were obtained to further quantify the chemical nature of nanostructures. The wide scan XPS spectra of TiO_2 on non-conducting (glass), conducting (ITO) substrates are shown in **Figure 2.13**. Detailed elemental analysis and peak fitting for surface state quantification from C1s and Ti2p was done as described as in the literature [118].

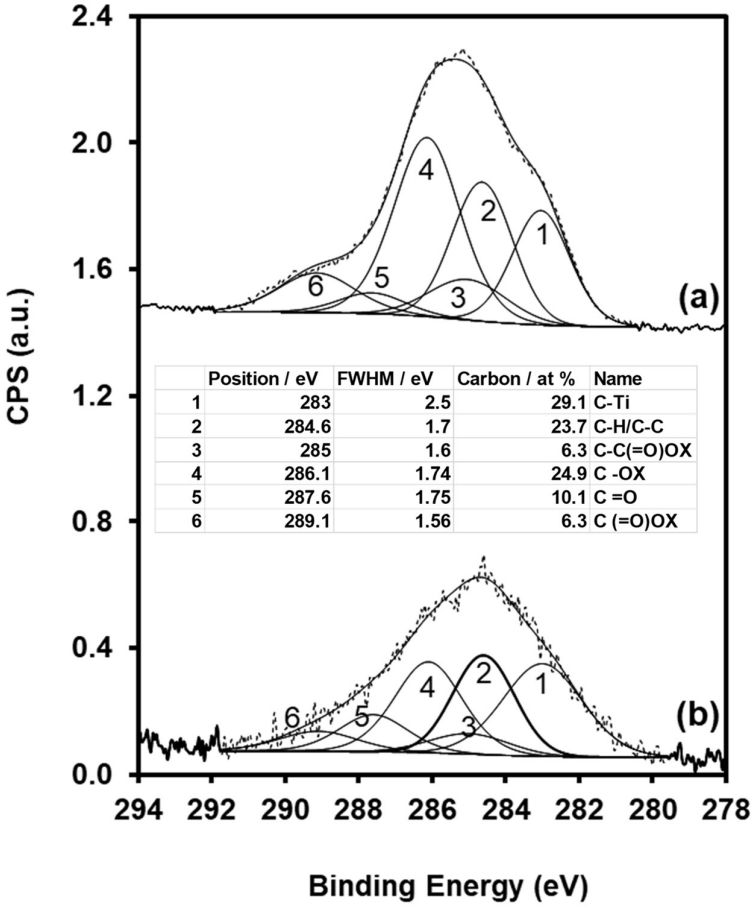

Figure 2.13: High resolution C1s XPS spectra of TiO_2 on (a) NCS and (b) CS.

The higher resolution C1s XPS spectra of TiO_2 film surface prepared on glass substrates was fitted with six peaks of different carbon environments as: C-Ti at 283± 0.3eV, hydrocarbon (C-H/C-C) at 284.6± 0.3 eV, (C-C(=O)OX) at 285± 0.2 eV, (C-OX) at 286.1± 0.3 eV, (C=O/O-C-O) at 287.6± 0.3eV and (C(=O)OX) at 289.1± 0.3 eV.

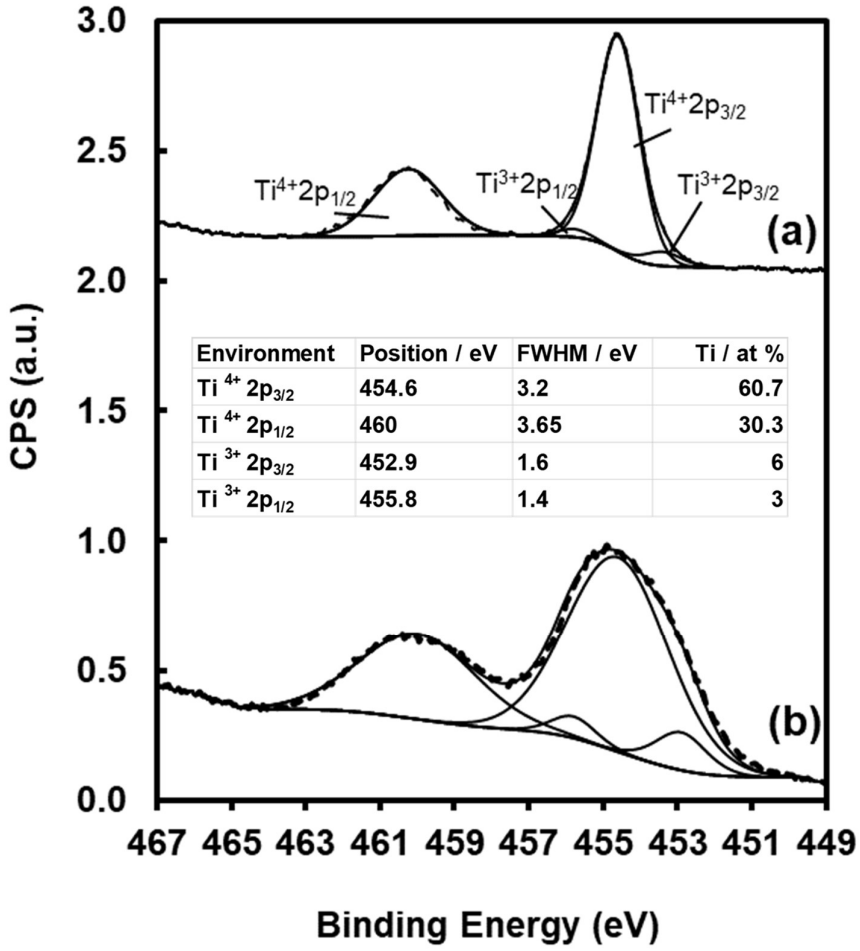

Environment	Position / eV	FWHM / eV	Ti / at %
Ti^{4+} $2p_{3/2}$	454.6	3.2	60.7
Ti^{4+} $2p_{1/2}$	460	3.65	30.3
Ti^{3+} $2p_{3/2}$	452.9	1.6	6
Ti^{3+} $2p_{1/2}$	455.8	1.4	3

Figure 2.14: High resolution Ti2p XPS spectra of TiO2 on (a) NCS and (b) CS.

TiO_2 films on glass showed a spectra shift of 0.51 eV towards lower binding energy side which was adjusted to its original position. This shift is expected due to charge accumulation on NCS by the bombardment of X-ray photons during XPS analysis which causes a positive charge to be accumulated as the electrons were ejected by the photo-electron effect.

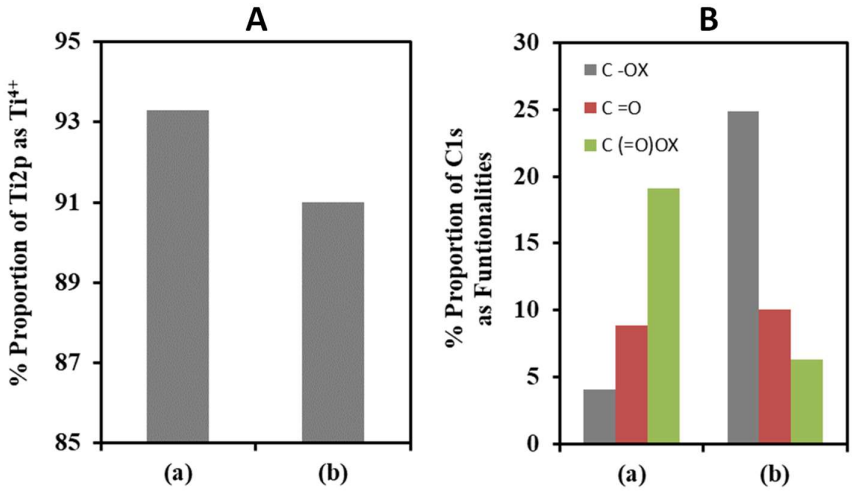

Figure 2.15: Relative variation in the % proportion of (A) Ti^{3+} in Ti2p XPS spectra and (B) COX, CO and C(=O)OX in C1s of TiO_2 (a) NCS and (b) CS.

This charge accumulation corresponded to the observed shift in the binding energy of 0.51 eV energy shift in the XPS spectra for the TiO_2 films grown on non-conducting substrates. The higher resolution C1s XPS spectra of TiO_2 film surface prepared on glass substrates was fitted with six peaks of different carbon environments as: C-Ti at 283± 0.3eV, hydrocarbon (C-H/C-C) at 284.6± 0.3 eV, (C-C(=O)OX) at 285± 0.2 eV, (C-OX) at 286.1± 0.3 eV, (C=O/O-C-O) at 287.6± 0.3 eV and (C(=O)OX) at 289.1± 0.3 eV. There was no spectral shift observed for TiO_2 nano-structures grown on conducting (ITO) glass substrates.

High-resolution Ti2p XPS spectra of TiO_2 gown on NCS and CS are shown in **Figure 2.14**. Different titanium oxidation states were quantified in the high-resolution Ti2p XPS spectra of TiO_2 nanostructures grown on ITO and glass substrates. The spectra were fitted with four peaks as $Ti^{3+}2p_{3/2}$ at 452.9± 0.4 eV, $Ti^{4+}2p_{3/2}$ at 454.6± 0.2 eV, $Ti^{3+}2p_{1/2}$ at 455.8± 0.4 eV and $Ti^{4+}2p_{1/2}$ at 460.0± 0.2 eV. TiO_2 nanostructures grown on ITO substrates showed significant increase in Ti^{3+} surface state of Ti2p. The relative increase substrates showed significant increase in Ti^{3+} surface state of Ti2p. The relative increase in the proportion of Ti2p surface

states indicates relative decrease in number of oxygen atoms surrounding to Ti atoms in these nanostructure assemblies. These observations are consistent with the atomic % proportion obtained from wide scan XPS spectra as well.

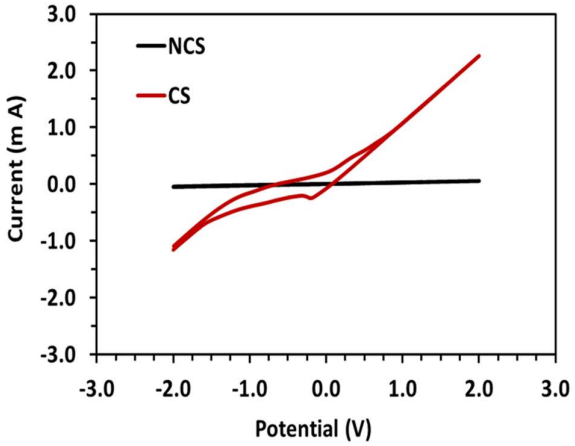

Figure 2.16: Nanostructures of TiO_2 grown on CS showed current conduction in cyclic voltammetry response whereas TiO_2 on NCS does not support charge conduction similar to CS conditions.

A relative variation in the % proportion of the different surfaces' states of C1s and Ti2p with different types of nano-structures film prepared on CS and NCS are shown in **Figure 2.15**. An increase in the Ti^{3+} surface states of Ti2p was obtained from TiO_2 nanostructures grown on CS substrate as compare to NCS. Mainly five different types of carbon surface states as C/C-H, C-C(=O)OX, C-OX, C=O and C(=O)OX were observed in TiO_2 films on all substrates. Here, we are interested to see the relative variation for three active functional groups C-OX, C=O and C(=O)OX present at the nano-surface obtained on CS and NCS. The percentage proportion of hydroxyl functional groups at the surface in TiO_2 nano-structures was significantly increased while the substrates were changed NCS to CS. There was no significant change in the % of carbon atoms as C=O in C1s at the surface of TiO_2 nano-

structures grown on different types of substrates. TiO_2 nano-structures grown on glass substrates show presence of maximum numbers of carboxylic acid functional groups.

Cyclic voltametric equipment was used to measure cyclic voltametric response of nanostructured TiO_2 on CS and NCS with three electrode system. CV response of nanostructured TiO_2 on these surfaces was quantified to assess the charge conductivity in liquid solutions using a three-electrode system (**Figures 2.16**). At positive bias voltage, during CV acquisition, charge conduction in TiO_2 nanostructured on CS show a linear increase in current with the increase of applied voltage. We did not observe any distinct oxidation peak for the TiO_2 on CS which indicates the charge stability of the nanostructured TiO_2 in electrolyte during the applied potential. During the negative bias voltage, we observed a slow increase in the current for the potential below -0.2V. We did not observe any significant change in the current of CV response for the nanostructured TiO_2 on NCS during both positive and negative bias voltage. Thus, nanostructured TiO_2 on CS facilitates dynamic charge neutralization of the TiO_2 surface while interacting with the overlying adhered stem.

2.5 Preparation of 2D coatings of functionally graded chitosan-gold nanocomposite

2.5.1 Methodology

Various studies had reported that the nanotechnology in health and medicine possess the potential to provide solutions for many complex and life-threatening diseases like cancer, neurodegenerative diseases, diabetes etc [119, 120]. These have been addressed by developing nanocomposites of polymers, metals and hybrid materials but the challenges still exist towards scalability of the processes developed in the laboratory,

stability, reproducibility and improving the essential nature of the desired materials by adopting various methods [120-134].

Impregnation of the nanoparticles in the biocompatible polymeric matrix have shown potential for surface coating, tailoring of surface interface properties and their stabilization for applications in different fields [135-138]. The impregnation of nanoparticles has limitations for achieving uniform distribution, retaining their functional characteristics and stability. Therefore, the current need is to develop a process which enables the formation of nanoparticles in an in-situ reduction process, to provide stable coordination with polymers of film forming capability and sustain possibility for changing surface interface characteristics. In the past, this has been addressed with the use of chitosan which has multiple roles as a reducing agent, stabilizer for metal ions [139, 140]. Additionally, chitosan is biodegradable, biocompatible, non-toxic biopolymer and possess biocidal characteristics which makes it suitable to be used in biological systems [141]. Thus, it is advisable to have a strategy for making cohesive polymer coating with ability in reducing the metal salt and converting these into nanoparticles through the in-situ reduction process.

Chitosan has the ability for reduction of metal salt and synthesis of nanoparticles but the role of different functional moieties within the chitosan chain in the reduction mechanism remains elusive [142-152]. Thus, ambiguity in the complexation of metal nanoparticle formation and involvement of oxygen and nitrogen atom containing functionalities of chitosan in reduction still prevails. To address above mentioned limitations, here we have contributed towards finding the role of cationic dominating ($-NH_3^+$) and anionic dominating ($-OR^-$) functionalities of chitosan in

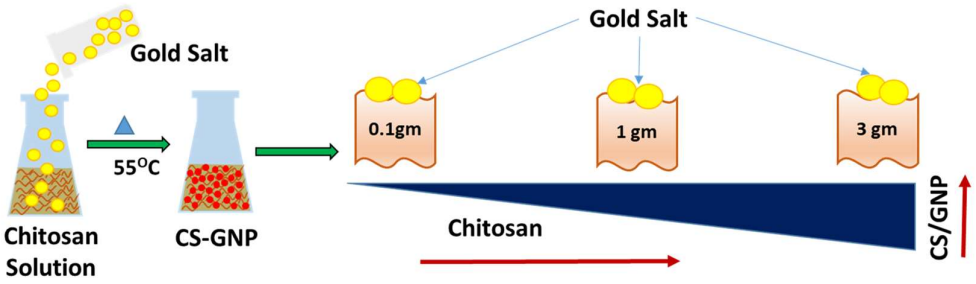

Figure 2.17: Schematic representation of preparation of CS-GNP composite films.

the reduction process of metal salts at different environments. Another important aspect of this study was to investigate the chemical and structural modifications in chitosan coating while it reduces gold chloride in cationic and anionic environments.

2.5.2 Preparation of functionally graded chitosan-gold platforms

A schematic representation of the process which was adopted for preparing coatings of CS-GNP nanocomposite and synthesis of GNP is shown in **Figure 2.17**. Different amount of (0.1 g to 3 g) chitosan powder in 100 ml of distilled water having 0.5% (v/v) of acetic acid were mixed separately. These separate solutions were kept at 55°C and provided with constant stirring at 300 rpm till a transparent solution was obtained. 15 ml from each of the different concentration of chitosan solutions were taken and drop wise addition of 0.4 mM of gold chloride was then done to them. Further, time-dependent kinetics of in-situ reduction of gold chloride and subsequent formation of gold nanoparticles was quantified by spectroscopic observation of surface plasmon resonance (SPR) of these particles. The SPR property of GNP was utilised to monitor the time dependent reduction of gold chloride by chitosan to understand the reduction process [153-156]. The experimental conditions were monitored in a time-dependent manner for three days to optimize the kinetics of the reduction process in chitosan gel solution.

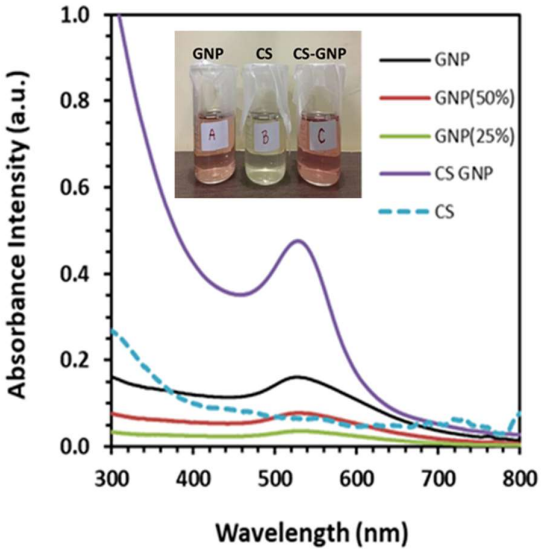

Figure 2.18: UV-Vis spectra where in the spectra GNP represents colloidal suspension of gold nanoparticles synthesized with chemical reduction, GNP (50%) represents dilution of GNP by addition of water to 50% and GNP (25%) represents dilution of GNP by addition of water to 75%. This dilution we performed to confirm that A_{SPR}/A_{450} does not change with dilution; where A_{SPR} and A_{450} are absorbance at GNP SPR peak and 450 nm, respectively. CS and CS-GNP, represent the spectra of chitosan and gold nanoparticle synthesized by chitosan reduction, respectively.

A gradual change in colour of these colloidal suspensions from light yellowish solution to pink was seen. This change confirms the formation of gold nanoparticles (GNP). After three days the functionally graded 2D films (depending on the chitosan-gold concentration and variation in spectroscopic characteristics) were made by casting the prepared chitosan colloidal suspension containing nanoparticles on tissue culture plastic surface by solvent evaporation method. This was achieved by keeping the plate in an incubator shaker at 50°C under constant shaking for 24 h. To compare SPR response, synthesis of GNP was also done with the use of lithium borohydride ($LiBH_4$) as reducing agent for similar concentrations of gold chloride [153]. The SPR characteristics information obtained from UV-vis spectra and these results were used for spectroscopic estimation of GNP concentration and determining their size in

colloidal suspension [154]. UV-Vis spectrum of a colloidal suspension of GNP (synthesized by chemical reduction [153] along with CS and CS-GNP colloidal suspension) is shown in **Figure 2.18.**

GNP was also diluted at two concentrations, 50 % (GNP (50%)) and 75% (GNP (25%)) for calculating the ratio of absorbance A_{SPR} and A_{450} at λ_{SPR} and λ_{450}, respectively where,λ_{SPR} indicates the wavelength at which surface plasmon resonance (SPR) of gold nanoparticles appears in the UV-Vis spectra while λ_{450} specifies absorbance at 450 nm. This was used for calculating the size of the GNP by spectroscopic observations using the mathematical model developed by Haiss et al. [155]. This model was used to estimate the diameter of nanoparticles by measuring the ratio of absorbance A_{SPR} and A_{450} at λ_{SPR} and λ_{450}, respectively.

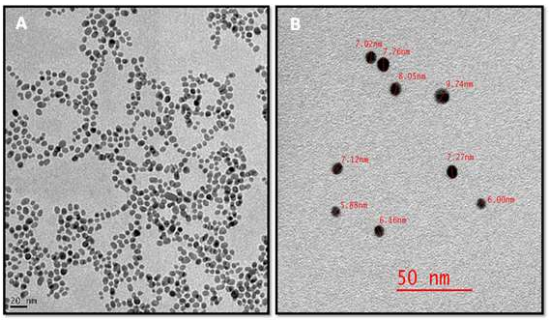

Figure 2.19: (A) TEM image of GNP synthesized with $LiBH_4$ reduction as synthesized in previous studies [42]. (B) TEM image showed dispersion of GNP within the chitosan network (size distribution marked in the range 5 nm to 10 nm).

The ratio of the A_{SPR} and A_{450} were 1.33 and 1.3 for the GNP and CS-GNP, respectively, as depicted in **Figure 2.18**. Thus, the spectroscopically calculated size of GPNs synthesized through chemical reduction and reduction by chitosan was ~6 nm. Molar concentration (C) = $A_{450}/\varepsilon_{450}$ of GNP was also calculated by using the molar extinction coefficient (ε_{450}) values from the same model [156]. The molar

concentration of these GNP was found to be in the order of 100 μM with an average particle size of 6 nm. Optical images of the CS, CS-GNP and GNP are also shown in **Figure 2.18** A clearly noticeable colour representing the presence of nanoparticle was visible in both the GNP and CS-GNP colloidal suspension. Size of the nanoparticles was ~7 nm in TEM image (**Figure 2.19**) of GNP which remains similar in TEM image of CS-GNP with a higher degree of uniformity in the size distribution, without agglomeration. Size measurement by both spectroscopic and TEM observation was found to be comparable.

2.5.3 Analysis of Temporal Progression for GNP-Chitosan Optical Characteristics

Chitosan solutions of various weights to volume ratio (0.1 g, 0.5 g, 1 g and 3 g) were prepared and these solutions were separately casted across the surface in tissue culture plates. This CS solution casted on TCP surfaces were allowed to stabilize for 1 h and after that, gold chloride solution at 0.4 mM was added uniformly added across the surface. Time-dependent UV-Vis spectra of these surfaces were obtained by microplate reader in absorbance mode to monitor the reaction kinetics between chitosan and gold chloride molecules at the surface and results are shown in **Figure 2.20 and Figure 2.21**. For the first 3 h, there was no significant change in the absorbance measured in UV-Vis spectrum. However, at higher time points, a noticeable change had started to appear in the absorbance intensity of the spectra corresponding to the SPR peak of GNP in the range 500 nm to 700 nm in the spectra which had shown a gradual increase with time.

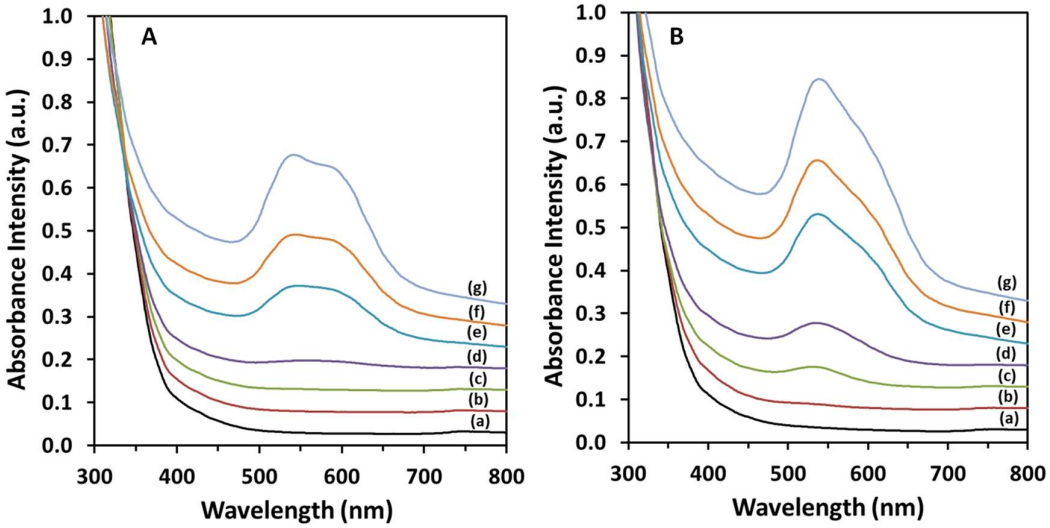

Figure 2.20: Time dependent UV-vis spectra of CS coating surface participating in in-situ reduction of gold chloride on tissue culture plastic surface with the use of (A) 0.1 g and (B) 0.5g, (C) 1g and (D) 3 g of chitosan in 100 mL solution. 0.4 mM of $AuCl_3$ used. a (t = 0 h), b (t = 6 h), c (t = 24 h), d (t = 30 h), e (t = 48 h), f (t = 54 h) and g (t = 72 h).

Low side of the used concentration of chitosan for the reduction of gold chloride had exhibited two peaks at 541 nm and in the spectra. The peak at 541 nm in the spectra becomes prominent with a shift in the second peak at 616 nm, 604 nm and 586 nm at 48 h, 54 h and 72 h, respectively for the use of 0.1 g of chitosan in 100 mL. Similarly, SPR peaks at 539 nm and 604 nm for 0.5 g and 536 nm and 578 nm for 1.0 g of chitosan in 100 mL solution were also observed. First observable SPR peak appeared after 6 h upon addition of gold chloride in the case of 1.0 g of chitosan (24 h for 0.5 g and 30 h for 0.1 g). Spectra showed the highest rate of GNP formation for the use of 1.0 g chitosan whereas a further increase in the chitosan concentration (3.0 g) resulted in the decrease in proportion and distribution of GNP formation with the time. Based on these results, it can be concluded that the polymer concentration played a key role in the nucleation of nanoparticles and its distribution.

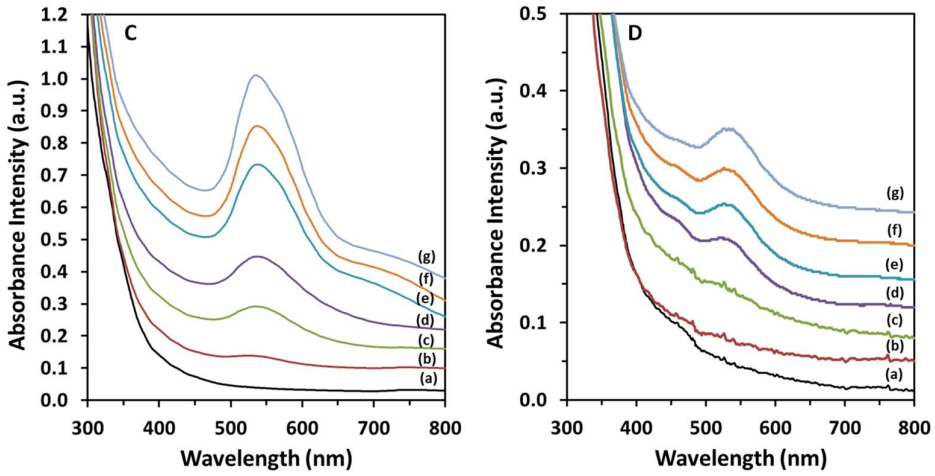

Figure 2.21: Time dependent UV-vis spectra of CS coating surface participating in in-situ reduction of gold chloride on tissue culture plastic surface with the use of (A) 1 g and (B) 3g, (C) 1g and (D) 3 g of chitosan in 100 mL solution. 0.4 mM of $AuCl_3$ used. a (t = 0 h), b (t = 6 h), c (t = 24 h), d (t = 30 h), e (t = 48 h), f (t = 54 h) and g (t = 72 h).

2.5.4 Crystallite structural analysis and size distribution of GNP in films of chitosan– GNP at various concentrations of CS

Figure 2.22A shows the X-ray diffractograms (XRD) of CS and CS-GNP films. CS film surface shows two distinct characteristic peaks at the 2θ value of 16.9° and 22.7° those corresponds to (002) and (101) crystallographic planes of chitosan, respectively. In comparison to chitosan, XRD patterns of CS-GNP film show a shift in characteristic peak (22.7°) of chitosan towards higher two theta with increased peak width and disappearance of peak at 16.9°. The broadening of peaks was also observed. This manifested chitosan crystallinity had changed to more amorphous phase which could be due to the incorporation of GNP into chitosan matrix. A dominating characteristic XRD peak of gold appeared at the 2θ value of 38.1° in CS-GNP films. This peak indicates preferential growth in the crystallographic planes (111) and a small peak at

2θ value of 44.3° was also observed, which corresponds to crystallographic planes (200) of gold. The XRD diffraction pattern coincided with that determined in previous literatures [157]. These represent face-centered cubic lattice of GNP in the film. A gradual increase in the proportion of peak intensity at 38.1° corresponding to gold in the XRD pattern was observed with an increase in CS concentration (0.1 g, 0.5 g and 1.0 g). At higher concentration (3.0 g) of chitosan, XRD spectra of CS-GNP films has shown weak appearance of distinct peaks corresponding to the gold.

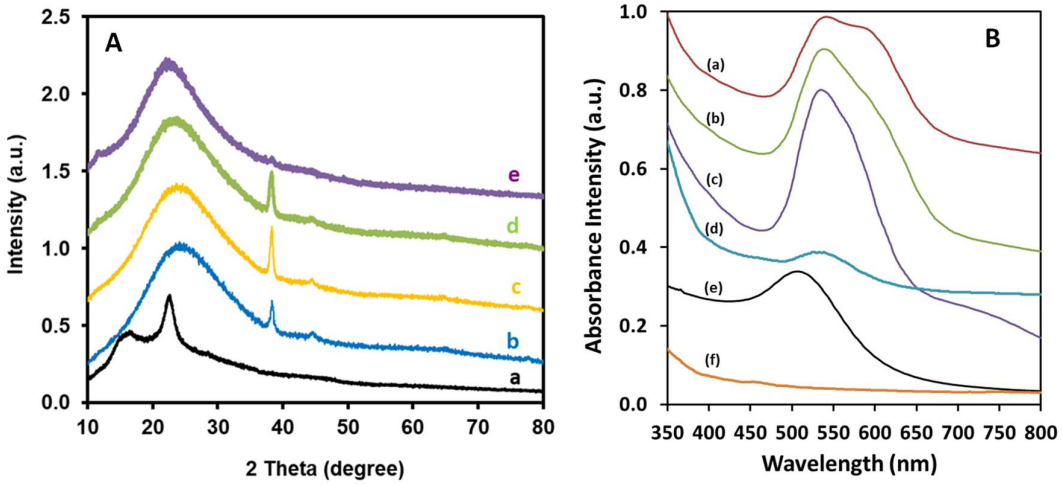

Figure 2.22: (A) XRD spectra of CS-GNP films at different concentrations of chitosan (a) chitosan without gold and (b-e) for 0.1 g, 0.5 g, 1 g, and 3 g of chitosan with gold chloride. (B) UV-vis spectra of CS-GNP films at different concentrations of chitosan (a-d) for 0.1 g, 0.5 g, 1 g, and 3 g of chitosan with 4mM gold chloride, (e) colloidal suspension of only GNP and (f) chitosan film without GNP. (C) Data obtained from spectroscopic analysis of size and concertation of GNP in CS-GNP film surface.

This observation was similar to the UV-Vis spectra in **Figure 2.22B,** where the reduction of gold chloride did not happen significantly at higher chitosan concentration. Size and molarity of the GNP corresponding to prominent SPR peak in CS-GNP films was obtained by measuring the ratio of absorbance at λ_{SPR} and λ_{450} [87] in spectroscopic observations of UV-Vis spectra. From the spectra, the average size of

the GNP was found between 30 nm to 14 nm for the use of 3.0 g to 0.1 g of chitosan. Molar concentration (C) of GNP in CS-GNP film was calculated by using the molar extinction coefficient (ε_{450}) values [140] with the use of formula $C = A_{450}/\varepsilon_{450}$. Relative change in particle size and their molar concentration is shown in Table 2.2.

***Table 2.2**: Size and concertation of GNP in CS-GNP film surface by spectroscopic analysis*

CS (%w/v)	$AuCl_3$ (mM)	λ_{spr} (nm)	A_{SPR}	A_{450}	A_{SPR}/A_{450}	D (nm)	ε_{450}	$C=A_{450}/\varepsilon_{450}$
0.1	0.4	542	0.611	0.358	1.71	20	5.41E+08	6.62E-10
0.5	0.4	539	0.654	0.398	1.64	16	2.67E+08	1.49E-09
1	0.4	536	0.92	0.568	1.62	14	1.76E+08	3.23E-09
3	0.4	546	0.167	0.091	1.84	30	1.96E+09	4.64E-11

2.5.5 Role of acidic and basic pH on the preparation of GNP-CS composites

Previously, several studies had suggested that the protonation of amine group ($-NH_3^+$) in the acidic environment plays a significant role in the reduction of gold chloride by chitosan and subsequent formation of GNP [131-133]. Therefore, an important aspect was to understand the mechanism for the reduction of gold chloride by chitosan. As it is known that the pKa value of reducing material is an important parameter and it had been previously reported that the pKa value of chitosan was in the ranges from 6.5-7.0 [158, 159]. So, the solution at pH below 6.5 results in protonation of amine group of chitosan. Henceforth, the experiments were designed to elucidate whether (i) protonated amine solely plays a role in the reduction process or (ii) even in its absence formation of GNP could be possible. This was achieved by performing the experiment at two completely different conditions of pH environment such as acidic (varying pH from 4.5 to 2.0), physiological (7.4 pH) and basic (varying pH from 9.5 to 12.0) and quantifying conditions which promotes formation of GNP in CS-GNP nanocomposite. UV-Vis spectroscopic analysis confirmed the formation of GNP in the varying acidic

pH range. Earlier studies reported the formation of GNP at acidic pH only, however, in this study, the role of both hydroxyl and amine functional moieties of CS were observed for the reduction of gold chloride. Thus, to further investigate the role of hydroxyl moieties of CS in reduction process, an experiment was carried out to find the possibility for the formation of GNP at basic condition.

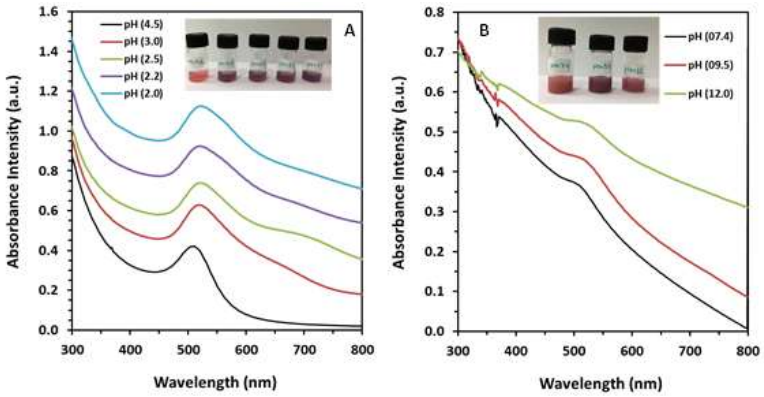

Figure 2.23: UV-Vis spectra with optical images of CS-GNP colloidal suspensions at (A) acidic pH values and (B) basic pH values.

UV-Vis spectroscopic analysis confirmed the formation of GNP at basic pH range. It was confirmed that the reduction process was occurring in both acidic ($-NH_3^+$ dominating, **Figure 2.23A**) and basic ($-OR^-$ dominating, **Figure 2.23B**) environments. In basic range, the transparent nature of CS was reduced, therefore, the UV-Vis spectra show a significantly reduced intensity of absorbance, hence spectra were obtained at five times diluted concentration with a quartz cuvette having a path length of 1 mm.

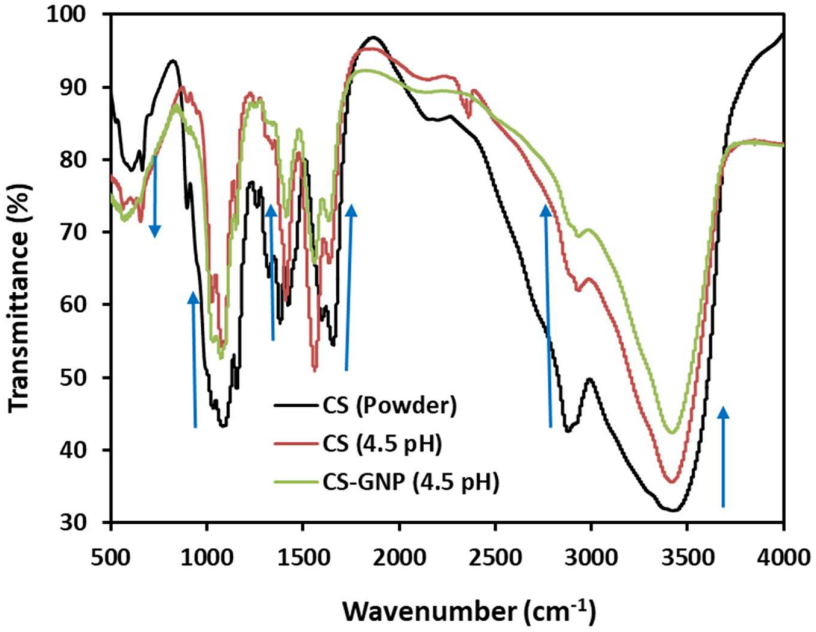

Figure 2.24: FTIR spectra of CS powder and colloidal suspension having 4.5 pH values of CS and CS-GNP during the synthesis.

FTIR spectra of the colloidal suspension of CS-GNP prepared at different pH was obtained to observe a relative change in corresponding functional moieties and to understand the role of these moieties in the reduction process. **Figure 2.24** shows the FTIR spectrum of CS powder and both CS solution and CS-GNP prepared at acidic pH. The FTIR spectrum of chitosan solution prepared at pH 4.5 which show an increment in % transmittance at 1579 cm^{-1} corresponding to amine group in comparison with spectra of CS powder. Protonation of the amine group of CS in the acidic environment results into a decrease in the proportion of this group as observed in the FTIR spectra. Further, a relative increase in the % transmittance at 1579 cm^{-1} was observed in the spectra of CS-GNP indicating the participation of amine group interaction with metal ions for GNP formation Due to the interaction

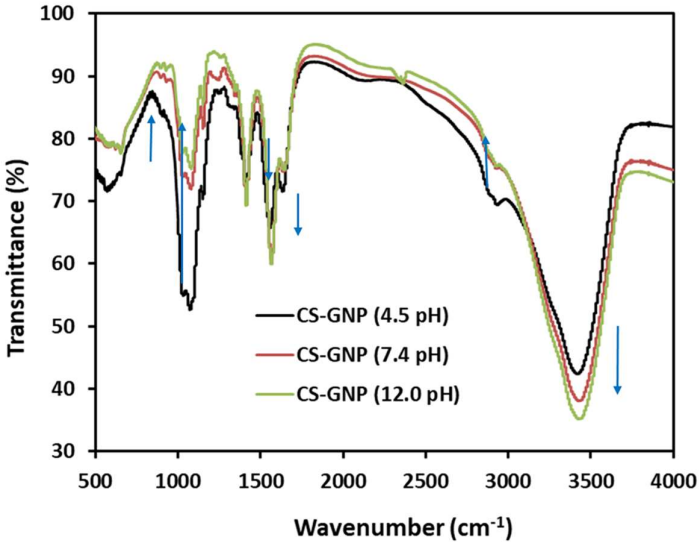

Figure 2.25: FTIR spectra of films prepared from the colloidal suspension having different basic pH values of CS-GNP during the synthesis.

of gold ion with groups containing nitrogen atoms in CS showed a relative change in % transmittance at wavenumbers corresponding to bonds associated with N atoms (N-H bending/stretching 1090 cm^{-1}, C-N stretching 1359 cm^{-1}, and N-H rocking 895 cm^{-1}) in CS-GNP. Previously, similar results were also reported where nitrogen containing functional moieties act as an active absorption site for the metal ion [160]. However, wide peak attributing to a hydroxyl group (3405 cm^{-1}) became weaker and sharper which indicated a significant role of this group in the formation of GNP. Another significant change was observed at the wavenumber of 2880 cm^{-1} ascribing C-H and O-H stretching. Thus, oxygen atoms in hydroxyl group could have interacted with gold ion. The FTIR spectra confirmed the role of both amine and hydroxyl group in the reduction process for the formation of GNP.

The FTIR peak corresponding to hydroxyl groups became significant as the pH increased, as shown in **Figure 2.25**. This significant decrease of transmittance in this band region indicated that -OH vibration played a salient role in gold ion adsorption

during the formation of GNP. FTIR spectra showed a noticeable change in the % transmittance corresponding to bonds associated with N atoms of CS-GNP while the solution pH was changed from acidic (4.5 pH) to basic (7.4 pH). No further significant change in the % transmittance in the FTIR spectra was observed at wavenumber 895 cm^{-1}, 1090 cm^{-1}, 1359 cm^{-1} and 1589 cm^{-1} bonds associated with N atoms of CS-GNP at different levels of basic pH (from 7.4 to 12). Therefore, the role of the amine group was minimum in formation of GNP at basic condition. Based on these results, it can be concluded that both nitrogen and oxygen atom can act as an immobilization site for gold atom by sharing their lone pair of electrons to initiate assembly of gold ions around it to form a metal complex.

Further to confirm the role of amine and hydroxyl group in the reduction process at acidic pH, ^{1}H NMR spectra of both CS and CS-GNP were performed by solubilizing chitosan in 0.5% deuterated acetic acid (CD_3COOD) in deuterated water (D_2O) for which the results are shown in **Figure 2.26**. The ^{1}H NMR spectrum presented the characteristic chitosan peaks at 2.1 ppm corresponding to three methyl proton of N-acetyl glucosamine (GlcNAc), 3.1-3.2 ppm represented H-b proton of glucosamine (GlcN). In the spectrum, peak at 1.7 ppm indicated protons of amine group while a broad range of signals from 3.5 to 4.0 ppm in the middle of the spectrum was observed due to partial overlapping of non-anomeric protons (H-c to H-f) having similar electron densities connected in the ring structure of glycosyl residue. The anomeric protons (H-a and H-g) overlapped with deuterated D_2O solvent peak thereby two peaks observed at 4.9 ppm and 4.6 ppm from H-a and H-g respectively. The NMR spectra obtained was coincident to studies suggested in

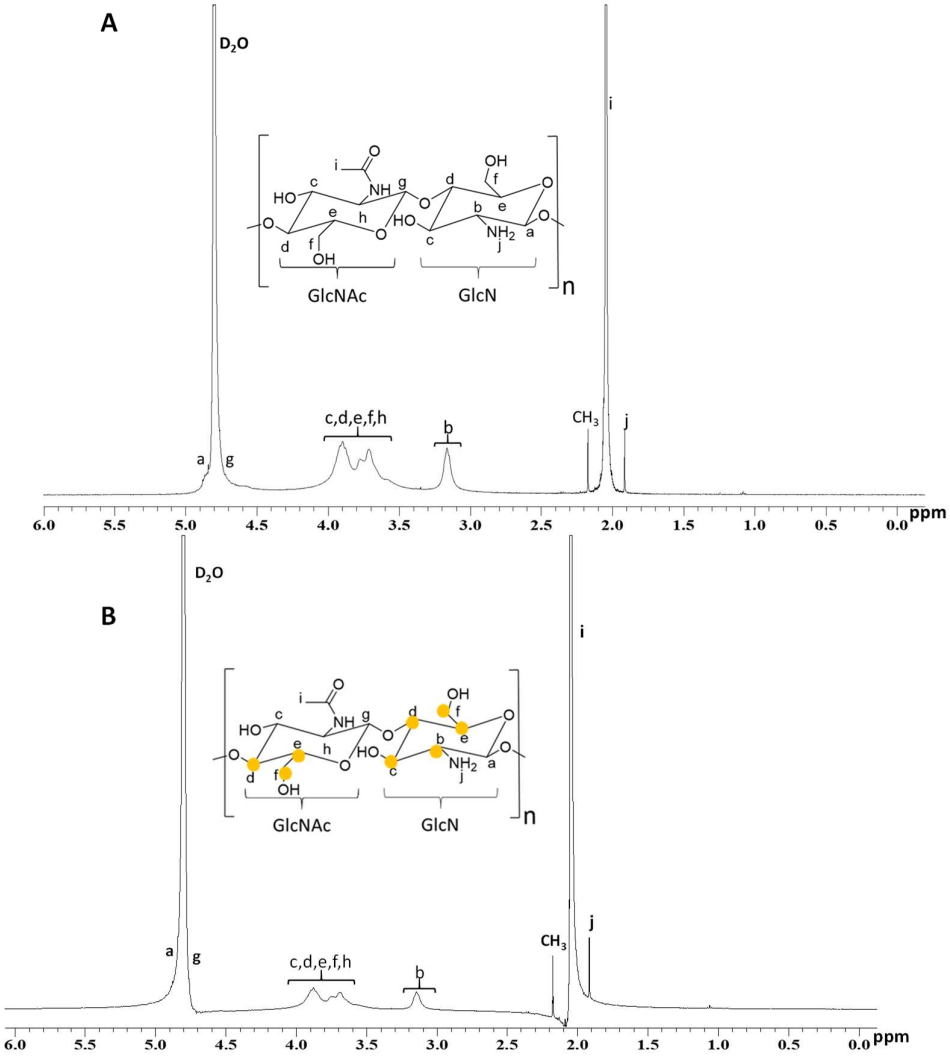

Figure 2.26: NMR spectra of colloidal suspension of (A) CS and (B) CS-GNP.

previous literatures [51,52]. The chemical shifts for residual protons of solvents were observed at 4.7 ppm for D_2O and 2.2 ppm for CD_3COOD. Based on the NMR spectra of CS-GNP, we can correlate reduction in NMR peaks of non-anomeric protons with conjugation and uniform dispersion of gold nanoparticles across the polymer matrix.

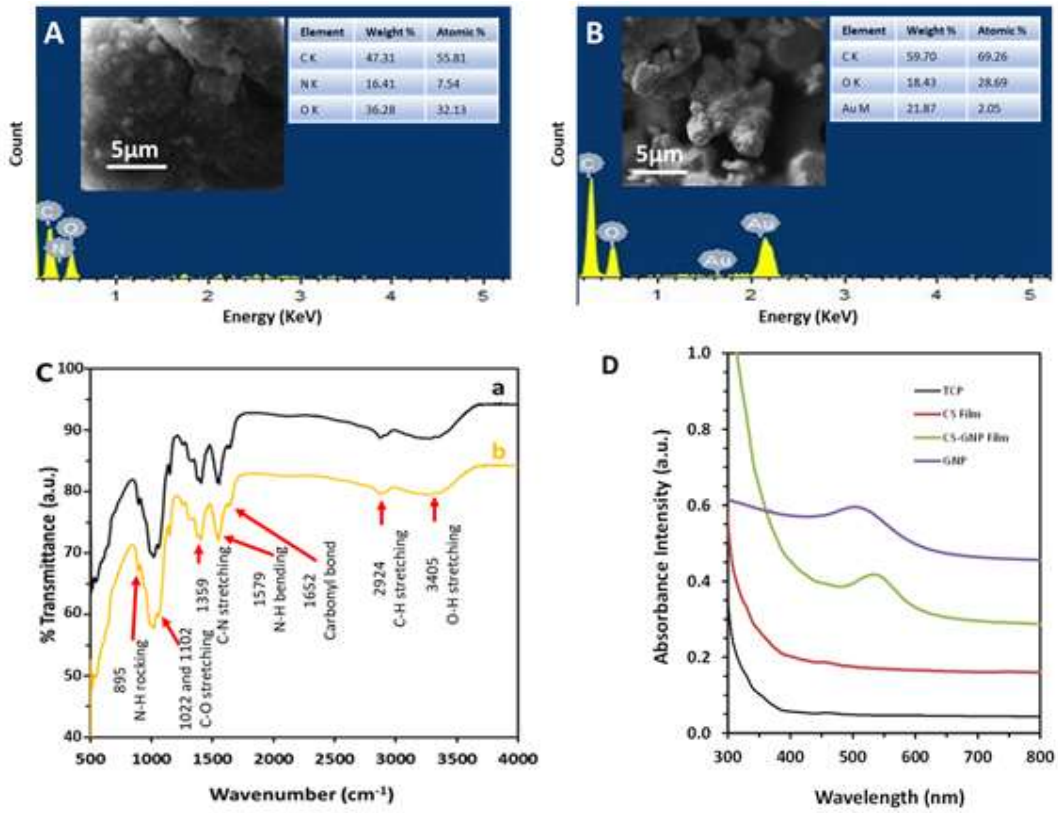

Figure 2.27: EDX spectra and FE-SEM image of (A) CS and (B) CS-GNP films, respectively. (C) ATR-FTIR spectra of CS (a) and CS-GNP (b) films. (D) UV-vis spectra of tissue culture plastic (TCP), CS films on TCP, CS-GNP film on TCP and GNP nano particle suspension.

2.5.6 Chemical composition and spectroscopic analysis of CS-GNP films

Films of CS and CS-GNP on a glass slide were obtained by solution casting from their respective colloidal suspensions after 72 h of reaction and drying by solvent evaporation method. Relative changes in surface morphology of chitosan film by incorporation of GNP was observed by SEM. Results for both CS and CS-GNP films surface morphology are shown in **Figure 27A**. Chitosan film surface displayed a heterogeneous morphology specifying a dense assembly with well-defined bright spots. Energy dispersive X-Ray spectroscopy (EDX) analysis of these spots (**Figure 27**) confirmed that they are composed of carbon, oxygen and nitrogen. Incorporation of GNP in chitosan led changes in the surface morphology and bright

spots were transformed to morphologically diverse representation of microstructures. This might be resulting from corresponding chemical changes during the reduction process and incorporation of GNP. EDX spectrum of CS-GNP showed a strong and typical optical absorption peak at 2.1 keV (Mα). This confirmed impregnation of metallic gold within the composite chitosan film. EDX spectra showed a significant presence of the gold.

Attenuated total reflection Fourier transform infrared (ATR-FTIR) spectra of the surface of CS and CS-GNP films on glass coverslips were obtained to get insights into molecular interaction between chitosan molecules and subsequent change by reduction of gold chloride (**Figure 27C**). ATR-FTIR spectra of CS showed peaks at 2924 cm^{-1} which indicated aliphatic C–H stretching; 1652 cm^{-1} corresponds to vibration of carbonyl bond (amide I) while peak at 1579 cm^{-1} corresponds to N–H bending of primary amine probably overlapped by N–H bending (amide II) of typical O=C–NHR groups and peak at 1359 cm^{-1} and 1318 cm^{-1} for C–N stretching (amide III band). The absorption peak 1102 cm^{-1} and 1022 cm^{-1} attributed to C–O stretching and peak at 895 cm^{-1} was due to N–H rocking vibrations. A strong and broad vibration band at 3405 cm^{-1} ascribed due to the overlapping of O–H and amine N–H stretching bands [46]. The most significant change occurring in ATR-FTIR spectra of CS-GNP was for the amino group band probably due to chitosan-metal ion molecule interactions. The spectra of CS-GNP composite showed a blue shift of peaks related to N–H bending, C–N stretching and N–H rocking vibration compared to pure polymer peaks. Here, the blue shift occurred due to electrostatic interaction between polymer and metal nanoparticles by sharing of lone pair of electrons between nitrogen and a metal cation. UV-Vis spectra of CS, CS-GNP films on tissue culture plastic surface (TCP) along with GNP colloidal suspension and TCP showed in **Figure 27D.** SPR peak corresponding to gold nanoparticle was observed at 535 nm and 514 nm for CS-GNP and GNP, respectively. A strong SPR peak corresponding to GNP at

535 nm in UV-Vis spectra of CS-GNP film confirmed the formation of GNP and their distribution in the composite film. Therefore, the synthesis of in-situ functionally graded chitosan-gold nanocomposite using gold salt and chitosan is a new approach for developing coatings on different substrates for applications in biomedical engineering. Though the process was slightly time consuming still, it had a significant advantage that it does not involve any hazardous component and hence such materials can be safe to use for biomedical applications in the future.